ACS OMEGA

http://pubs.acs.org/journal/acsodf

Article

$Ba_{33}Zn_{22}Al_8O_{67}$ with a Framework of $([O(Zn/Al)_4]/Ba)(Zn/AlO_4)_4$ Motifs

Rayko Simura,* Kyosuke Sawamura, Hisanori Yamane, and Takuji Ikeda

Cite This: *ACS Omega* 2021, 6, 30140−30147

Read Online

ACCESS | Metrics & More | Article Recommendations | Supporting Information

ABSTRACT: Single crystals of a new oxide, $Ba_{33}Zn_{22}Al_8O_{67}$ (melting point = 1452 K), were grown in a melt-solidified sample prepared by heating a compact of a $BaCO_3$, ZnO, and Al_2O_3 mixed powder in a dry airflow. $Ba_{33}Zn_{22}Al_8O_{67}$ can be handled in dry air, but it decomposes into carbonates, hydroxides, and hydrates in humid air. Single-crystal X-ray structure analysis clarified that $Ba_{33}Zn_{22}Al_8O_{67}$ crystallizes in a cubic cell (a = 16.3328 (3) Å, space group $F23$) having a three-dimensional Zn/AlO_4 framework in which $\{([OZn_4]/Ba)(Zn/AlO_4)_4\}$ motifs are connected to each other by bridging Zn/AlO_4 tetrahedra. A Ba atom or a $[OZn_4]$ cluster is statistically situated at the center of the motif with a probability of 0.5. Motifs of another type, $\{([O(Zn/Al)_4])(Zn/AlO_4)_4\}$, are isolated from the Zn/AlO_4 framework. These motifs, $\{([OZn_4]/Ba)(Zn/AlO_4)_4\}$ and $\{([O(Zn/Al)_4])(Zn/AlO_4)_4\}$, are alternatingly arranged along the a axis like a checkered cube, and Ba atoms are situated between the motifs. A linear thermal expansion coefficient of 10.4×10^{-6} K^{-1} was measured in an Ar gas flow at 301−873 K for a sintered $Ba_{33}Zn_{22}Al_8O_{67}$ polycrystalline sample with a relative density of 73%. A relative permittivity of 31 and a temperature coefficient of 15 ppm K^{-1} at 301 K were obtained for another sintered sample (relative density = 70%) in a dry airflow. The electrical conductivity at 1073 K and the activation energy for conduction at 923−1073 K measured for the sintered samples in dry and wet airflows were 6.2×10^{-7} S cm^{-1} and 0.65 eV and 2.9×10^{-6} S cm^{-1} and 0.59 eV, respectively.

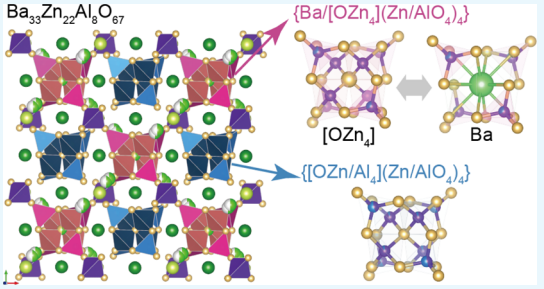

1. INTRODUCTION

In many metal oxides, an M-centered oxygen tetrahedron (MO_4), in which a cation (M^{n+}) is coordinated by four oxide anions (O^{2-}), is one of the important building blocks of their crystal structures, and chains, layers, rings, and networks are constructed by sharing the vertex O^{2-} ions of the MO_4 tetrahedra.[1,2] In the case of silicates and phosphates containing SiO_4 and PO_4 tetrahedra, only two MO_4 tetrahedra can share a single vertex O^{2-} because of the high valences of the M cations Si^{4+} and P^{5+}. However, in the case of MO_4 with lower-valence cations such as Zn^{2+}, more than two MO_4 tetrahedra can share a single vertex O^{2-}. When a vertex O^{2-} is shared with four MO_4 tetrahedra, an O^{2-}-centered cation tetrahedron, $[OM_4]$, can also be considered as a structural unit.[3,4] Recently, a systematic classification of some metal oxides having a structural component with an O^{2-}-centered Zn tetrahedron, $[OZn_4]$, has been proposed.[5] $[OZn_4]$-centered motifs of $\{[OZn_4]_x[MO_4]_y\}^{n-}$ are formed via the coordination of several MO_4 to a $[OZn_4]$ tetrahedron, and cations of alkali- and alkaline-earth-metal elements are located between the motifs. Bakakin and Seryotkin proposed two categories based on the valences of the $[OZn_4]$-centered motifs.[5] The first category comprises lower-valence motifs such as $\{[OZn_4]_2[(P \text{ or } As)O_4]_6\}^{6-}$, included in alkali-metal phosphate/arsenate hydrates such as $K_3Zn_4O(PO_4)_3{\cdot}4(H_2O)$, $Cs_3Zn_4O(PO_4)_3{\cdot}4(H_2O)$, and $Li_3Zn_4O(AsO_4)_3{\cdot}6(H_2O)$.[6] The second category comprises the higher-valence motifs $\{[O(Zn/Fe/Al)_4]_2[(Al_{0.8}Zn_{0.2})O_4]_6\}^{14-}$ and $\{[OZn_4]_2((Al_{0.87}Zn_{0.13})O_4)_6(Al_{0.87}Zn_{0.13})_5O_4\}^{18.4-}$, included in transition-metal aluminates and gallates such as tululite ($Ca_{14}(Fe^{3+},Al)(Al,Zn,Fe^{3+},Si,P,Mn,Mg)_{15}O_{36}$),[7] $Ca_{14}Al_{10}Zn_6O_{35}$,[8] and $Ca_{14}Zn_{5.5}Ga_{10.5}O_{35.25}$.[9] In the present study, a new compound having $\{([OZn_4]_{0.5}/Ba_{0.5})[(Zn_{0.67}/Al_{0.33})O_4]_4\}^{18.7-}$ and $\{([O(Zn_{0.92}/Al_{0.08})_4])[(Zn_{0.42}/Al_{0.58})O_4]_4\}^{15.4-}$ motifs was found in the Ba−Zn−Al−O system. A $[OZn_4]$ tetrahedral unit or Ba atom is located at the center of the $\{([OZn_4]_{0.5}/Ba_{0.5})[(Zn_{0.67}/Al_{0.33})O_4]_4\}^{18.7-}$ motif with a probability of 0.5. The synthesis, crystal structure, thermal expansion, and electronic properties of the new oxide are reported.

2. RESULTS AND DISCUSSION

2.1. Crystal Structure. The chemical composition measured by electron microprobe analysis (EPMA) for the single-crystal fragment obtained from the transparent part of

Received: September 18, 2021
Accepted: October 13, 2021
Published: October 27, 2021

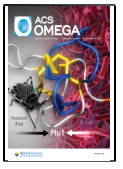

the melt-solidified sample was Ba 63(1), Zn 19(1), Al 2.7(4), and O 15(1) mass % (total 99.7(1) mass %). X-ray diffraction (XRD) spots were indexed using a cubic lattice parameter a = 16.3328(3) Å. The possible space groups suggested by systematic extinction rules were $Fm\bar{3}$, $F23$, $F\bar{4}3m$, $Fm\bar{3}m$, $F432$. The crystal structure was analyzed using a model of space group $F23$ having three Ba sites (Ba1−3), one mixed site (Ba4/O1) in which Ba and O statistically occupy, one Zn site (Zn1) that coordinates to the O1 site, four Zn/Al sites (Zn/Aln (n=2−5)) statistically occupied by Zn and Al, and five O sites (O2−6). A Ba:Zn:Al:O atomic ratio of 66:44:16:134 was obtained by refinement of the occupancies for Zn1, Zn/Al2−5, and Ba4/O1. This ratio corresponds to a composition of Ba 62.4, Zn 19.8, Al 3.0, and O 14.8 mass %, consistent with the EPMA results within the experimental error. On the basis of these results, the chemical formula of the new oxide was determined to be $Ba_{33}Zn_{22}Al_8O_{67}$ (Z = 2).

The occupancy parameters for Ba and O in Ba4/O1 (multiplicity and Wyckoff letter, 4c) and Zn in Zn1 (16e) converged to ∼0.5 and were therefore fixed at 0.5 in the following refinement. At this stage, the $R1$ (all data) was 3.5% with large anisotropic displacement parameters for Ba3, and then the Ba3 site was split into two sites, Ba3a (16e) and Ba3b (16e). The occupancies of these two split sites also became ∼0.5 and thus the occupancies of Ba3a and Ba3b were also fixed at 0.5 and 0.5. The shape of the anisotropic displacement ellipsoid for O4 situated at the original position of 16e was flat and spread on {111} planes. Therefore, O4 was placed at a general position (48h) with an occupancy of 0.3333. The $R1$ (all data) for the final refinement was 1.2%. A summary of the single-crystal X-ray structure analysis results is presented in Table 1. The coordination, occupancies, and equivalent isotropic atomic displacement parameters are listed in Table 2. The anisotropic atomic displacement parameters and the interatomic distances are listed in Tables S1 and S2 (Supporting Information).

As shown in Figure 1, the Zn^{2+} and Al^{3+} cations in Zn1, Zn/Al2, Zn/Al3, Zn/Al4, and Zn/Al5 are coordinated by four O atoms, forming Zn-centered and Zn/Al-centered O tetrahedra (ZnO_4 and Zn/AlO_4, respectively). The average atomic distances are 1.974 Å (Zn1−O), 1.968 Å (Zn/Al2−O), 1.865 Å (Zn/Al3−O), 1.908 Å (Zn/Al4−O), and 1.943 Å (Zn/Al5−O) (Table S2). These distances are plotted on a line connecting the interatomic distances for Al−O and Zn−O calculated from Shannon's effective ionic radii (Figure 2).[12]

Motifs composed of ZnO_4 and Zn/AlO_4 tetrahedra are recognized in the structure of $Ba_{33}Zn_{22}Al_8O_{67}$. In a motif, four Zn/Al2O6$(O2)_3$ tetrahedra connect to each other by sharing an O atom at O6; in addition, four Zn/Al3$O_4(O2)_3$ tetrahedra connect to the central Zn/Al2O6$(O2)_3$ tetrahedra by sharing an O atom at O2 (Figure 1a). This motif can be explained with an O6-centered $(Zn/Al2)_4$ tetrahedron, $[O6(Zn/Al2)_4]$, which is indicated with dotted red lines in this figure, and four Zn/Al3-centered $(O2)_3O_4$ tetrahedra, $[Zn/Al3(O2)_3O_4]$, around the $[O6(Zn/Al2)_4]$ tetrahedron. This motif is expressed as $\{[O6(Zn/Al2)_4][Zn/Al3O_4]_4\}$. The other motifs, $\{Ba4[Zn/Al4O_4]_4\}$ and $\{[O1(Zn1)_4][Zn/Al4O_4]_4\}$, statistically exist at the same position with 50% probability and are collectively denoted as $\{Ba4/[O1(Zn1)_4][Zn/Al4O_4]_4\}$. Ba4 is at the center of the $\{Ba4[Zn/Al4O_4]_4\}$ motif (Figure 1b). The O1-centered Zn1 tetrahedron, $[O1(Zn1)_4]$ is at the center of the $\{[O1(Zn1)_4][Zn/Al4O_4]_4\}$ motif and also surrounded by four Zn/Al4O5$(O3)_4$ tetrahedra (Figure 1c). The O atom at O3 is shared by Zn/Al4O5$(O3)_4$ and Zn1O1$(O3)_4$ tetrahedra. The atomic arrangement of the latter motif, $\{[O1(Zn1)_4][Zn/Al4O_4]_4\}$ is similar to that of $\{[O6(Zn/Al2)_4][Zn/Al3O_4]_4\}$. A motif containing an O-centered cation-coordinated tetrahedron at the center of the motif has also been reported for $Ca_{14}Zn_{5.5}Ga_{10.5}O_{35.25}$.[9] This compound has a $\{[OZn_4][Ga/AlO_4]_6\}$ motif in which six Ga/AlO_4 tetrahedra connect to the central $[OZn_4]$ tetrahedron.[5]

Using these motif expressions, we can write the crystal structure of $Ba_{33}Zn_{22}Al_8O_{67}$ as $Ba_{61}(Zn_{0.94}Al_{0.06})_4\{Ba_{0.5}[OZn_4]_{0.5}[Zn_{0.67}Al_{0.33}O_4]_4\}_4\{[O(Zn_{0.92}Al_{0.08})_4][Zn_{0.42}Al_{0.58}O_4]_4\}_4$. The formal charges of the motifs depend on the occupancies of Zn and Al and are in the range $\{[OAl_4][AlO_4]_4\}^{10-}$ to $\{[OZn_4][ZnO_4]_4\}^{18-}$ and $\{Ba[AlO_4]_4\}^{18-}$ to $\{Ba[ZnO_4]_4\}^{22-}$; the average charges of $\{[O(Zn_{0.92}Al_{0.08})_4][Zn_{0.42}Al_{0.58}O_4]_4\}$ and $\{Ba_{0.5}[OZn_4]_{0.5}[Zn_{0.67}Al_{0.33}O_4]_4\}$ are −15.4 and −18.7, respectively. These motifs can be related to the $\{[OM_4]_2[M'O_4]_6\}$ motif categorized as a high-valence motif with formal charges from −14 to −19.[5]

The $\{(Ba4/[O1Zn1_4])[Zn/Al4O_4]_4\}$ motifs are connected to each other via Zn/Al5$(O5)_4$ regular tetrahedra by sharing O atoms at O5 of Zn/Al5$(O5)_4$ and Zn/Al4O5$(O3)_3$ tetrahedra of the motifs, forming a three-dimensional network (Figure 3). The $\{([O6(Zn/Al2)_4])[Zn/Al3O_4]_4\}$ motifs are isolated from this network. As shown in Figure 3, the $\{([O6(Zn/Al2)_4])(Zn/Al3O_4)_4\}$ and $\{(Ba4/[O1(Zn1)_4])(Zn/Al4O_4)_4\}$ motifs

Table 1. Summary of the Crystal Structure Analysis Results for $Ba_{33}Zn_{22}Al_8O_{67}$

chemical formula, Z	$Ba_{33}Zn_{22}Al_8O_{67}$, 2
formula weight, M/g mol^{-1}	7258.2
form, color	granule, colorless
size, l/mm	0.09 × 0.08 × 0.07
temperature, T/K	301(2)
crystal system, space group (number)	cubic, $F23$ (196)
unit-cell dimensions, a/Å	16.3328(3)
unit-cell volume, V/Å^3	4356.9(2)
calculated density, D_{cal}/Mg m^{-3}	5.53
radiation type and wavelength, λ/Å	Mo $K\alpha$, 0.71073
absorption correction	multi-scan, SADABS[10]
absorption coefficient, μ/mm^{-1}	20.72
limiting indices	$-25 < h < 25$, $-25 < k < 25$, $-25 < l < 25$
$F000$	6296
θ range for data collection, deg	$2.16 < \theta < 33.04$
reflections collected, unique	52590, 1401
R_{int}	0.0315
data, parameters, restraints	1401, 68, 1
weight parameters[b], a, b	0.0045, 37.3422
[a]$R1$,[b]$wR2$,[c]S ($I > 2\sigma(I)$)	0.012, 0.025, 1.138
[a]$R1$,[b]$wR2$,[c]S (all data)	0.012, 0.025, 1.138
largest diff. peak and hole, $\Delta\rho$/eÅ^{-3}	0.91, −0.88
absolute structure parameter,[d] x	0.029(10)

[a]$R1 = \Sigma||F_o| - |F_c||/\Sigma|F_o|$. [b]$wR2 = [\Sigma w(F_o^2 - F_c^2)^2/\Sigma(wF_o^2)^2]^{1/2}$, $w = 1/[\sigma^2(F_o^2) + (aP)^2 + bP]$, where F_o is the observed structure factor, F_c is the calculated structure factor, σ is the standard deviation of F_c^2, and $P = (F_o^2 + 2F_c^2)/3$. [c]$S = [\Sigma w(F_o^2 - F_c^2)^2/(n-p)]^{1/2}$, where n is the number of reflections and p is the total number of parameters refined. [d]Absolute structure parameter (Flack parameter), x, is determined using 630 quotients $[(I+) - (I-)]/[(I+) + (I-)]$.[11]

https://doi.org/10.1021/acsomega.1c05190
ACS Omega 2021, 6, 30140−30147

Table 2. Fractional Atomic Coordinates and Equivalent Isotropic Displacement Parameters (Å^2) for $Ba_{33}Zn_{22}Al_8O_{67}$

label	site	occupancy	x	y	z	U_{eq} [a]
Ba1	24*g*	1	0.00205(3)	0.25	0.25	0.01810(6)
Ba2	24*f*	1	0.20530(2)	0	0	0.01250(5)
Ba3a	16*e*	0.5	0.40608(4)	0.40608(4)	0.40608(4)	0.0176(2)
Ba3b	16*e*	0.5	0.42322(4)	0.42322(4)	0.42322(4)	0.0318(3)
Ba4/O1	4*c*	0.5/0.5	0.25	0.25	0.25	0.0294(4)
Zn1	16*e*	0.5	0.31831(4)	0.31831(4)	0.31831(4)	0.0089(2)
Zn/Al2	16*e*	0.9211/0.0789(3)	0.82114(3)	0.82114(3)	0.82114(3)	0.0120(2)
Zn/Al3	16*e*	0.4204/0.5796(3)	0.63625(4)	0.63625(4)	0.63625(4)	0.0119(2)
Zn/Al4	16*e*	0.6742/0.3258(3)	0.13649(3)	0.13649(3)	0.13649(3)	0.0109(2)
Zn/Al5	4*a*	0.937/0.063(2)	0	0	0	0.0115(2)
O2	48*h*	1	0.1128(2)	0.2465(2)	0.6128(2)	0.0215(6)
O3	48*h*	1	0.1117(2)	0.1116(2)	0.2477(2)	0.0195(6)
O4	48*h*	0.3333	0.577(4)	0.581(2)	0.561(3)	0.025(8)
O5	16*e*	1	0.0687(2)	0.0687(2)	0.0687(2)	0.0165(8)
O6	4*d*	1	0.75	0.75	0.75	0.017(2)

[a] $U_{eq} = 1/3\ (U_{11} + U_{22} + U_{33})$.

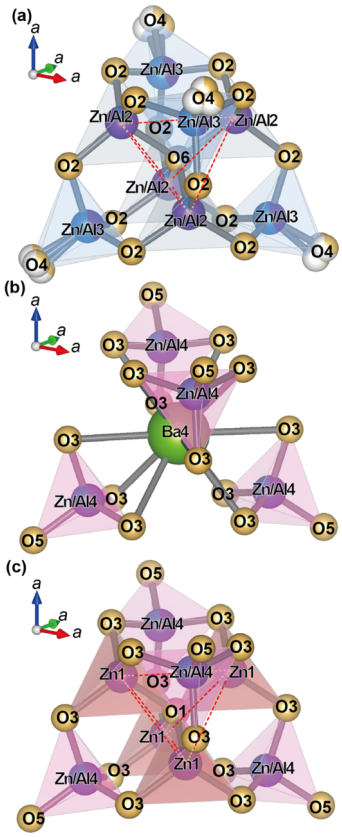

Figure 1. Atomic arrangements of the (a) {[O6(Zn/Al2)$_4$][Zn/Al3O$_4$]$_4$} motif, (b) {Ba4[Zn/Al4O$_4$]$_4$} motif, and (c) {[O1Zn1$_4$][Zn/Al4O$_4$]$_4$} motif. The dotted red lines in (a,c) indicate the central tetrahedron of [O6(Zn/Al2)$_4$] and [O1Zn1$_4$], respectively.

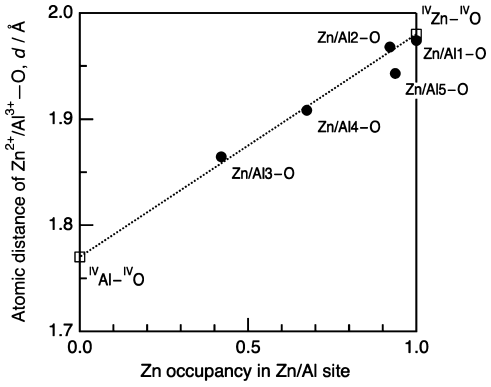

Figure 2. Interatomic distances for Zn/Al−O versus Zn occupancy in tetrahedral sites. Solid circles are Zn/Al−O distances in $Ba_{33}Zn_{22}Al_8O_{67}$, and open squares are Al−O and Zn−O interatomic distances calculated from Shannon's effective ionic radii.

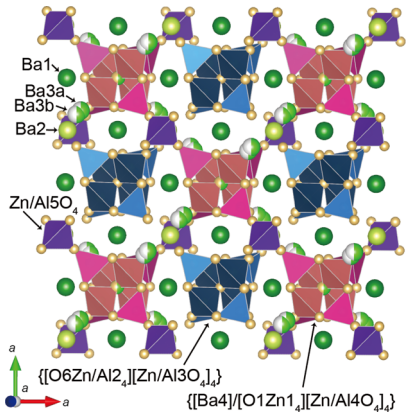

Figure 3. Crystal structure of $Ba_{33}Zn_{22}Al_8O_{67}$ illustrated for $0 < z < 0.5$ with {[O6Zn/Al2$_4$][Zn/Al3O$_4$]$_4$} motifs and statistical motifs of {Ba4/[O1Zn1$_4$][Zn/Al4O$_4$]$_4$}.

are alternatingly arranged along the *a*-axis direction like a checkered cube. Ba atoms at Ba1, Ba2, Ba3a, and Ba3b are aligned around the motifs.

The Ba atoms at Ba1 are in a cuboid arrangement (Figure 4) and are coordinated by eight O atoms with an average Ba1−O distance of 2.903 Å (Table S2). Four O atoms are at O2 of the {[O6(Zn/Al2)$_4$][(Zn/Al3O4)$_4$]} motif, and the other four O atoms are at O3 of the {Ba4/[O1Zn1$_4$](Zn/Al4O$_4$)$_4$} motif. Ba2 is in a distorted gyrobifastigium of eight O atoms: four O atoms at O2 and O4 of two {[O6(Zn/Al2)$_4$][Zn/Al3O$_4$]$_4$} motifs and four O atoms at O3 and O5 of two {Ba4/[O6(Zn/Al5)$_4$][Zn/Al3O$_4$]$_4$} motifs with an average Ba2−O distance of 3.032 Å. The Ba3 site is in the antiprism of three O atoms at O3 of one {Ba4/[O6(Zn/Al5)$_4$][Zn/Al3O$_4$]$_4$} motif and three O atoms at O4 of three {[O5(Zn/Al1)$_4$][Zn/Al2O$_4$]$_4$} motifs,

https://doi.org/10.1021/acsomega.1c05190
ACS Omega 2021, 6, 30140−30147

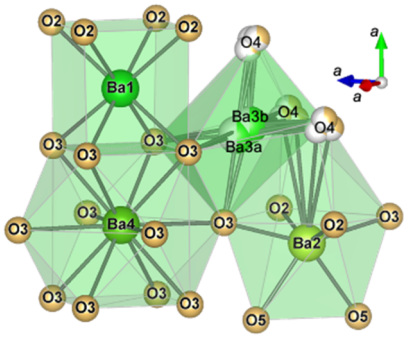

Figure 4. Atomic arrangement of O atoms around Ba atoms in $Ba_{33}Zn_{22}Al_8O_{67}$.

with Ba3a−O and Ba3b−O average distances of 2.693 and 2.714 Å, respectively. These Ba−O distances are comparable to the average Ba−O distances of $BaAl_2O_4$ (2.897 Å)[13] and $BaZnO_2$ (2.785 Å)[14] in six-fold coordination.

Ba4 is at the center of the $\{Ba4[Zn/Al4O_4]_4\}$ motif and in a cuboctahedron (Figure 4) surrounded by 12 O atoms. The Ba4−O (×12) distance is 3.197 Å, which is the longest of the Ba−O distances in O polyhedra of $Ba_{33}Zn_{22}Al_8O_{67}$ and is similar to the distances of 3.18, 3.16, and 3.18 Å reported for Ba in similar cuboctahedra with 12-fold coordination environments in $BaNdGaZn_3O_7$,[15] $BaCaCo_3ZnO_7$,[16] and $BaCa(Zn_{1-x}Fe_x)_4O_7$,[17] respectively.

2.2. Al Atom Distribution and Local Structure. 1-dimensional ^{27}Al DE-MAS NMR spectrum of $Ba_{33}Zn_{22}Al_8O_{67}$ (Figure 5a) reveals two resonance peaks at 79.2 and 84.9 ppm, which are characteristic of Al in four-fold coordination with O (i.e., AlO_4). The positions of the peaks (chemical shifts, δ) are similar to those in the spectrum of Al-doped ZnO powder.[18−20] In previous studies, the chemical shifts were interpreted as some of the tetrahedral Zn sites being substituted by Al atoms, where the observed Al environment can be described as a $Q^4(4Zn)$ configuration. In the present study, $Q^n(mT)$ is defined as follows: Q is the tetrahedral Al, n is the degree of condensation, T is a second neighboring tetrahedral atom (Al or Zn), and m is the number of bonding T atoms via oxygen.

Because the two resonance peaks overlap each other substantially in Figure 5a, we recorded the corresponding ^{27}Al 3QMAS spectrum. Two independent resonance peaks, **A** and **B**, were observed (Figure 5b), suggesting that Al atoms in $Ba_{33}Zn_{22}Al_8O_{67}$ can be classified into two local AlO_4 environments. The spectral widths along the F2 axis for both peaks are elongated by the substantial quadrupolar interaction. In addition, the large resonance peak **A** is broadened along the F1 axis, indicating that several resonance peaks associated with different local structures are overlapped.

For convenience, quadrupolar fitting was carried out for the resonance peaks. Several fitting parameters are summarized in Table S3. The resonance peak **A** was deconvoluted into three components at δ_{iso} = 80.9, 81.8, and 83.7 ppm. Given the low Al content in $Ba_{33}Zn_{22}Al_8O_{67}$, most of the peak **A** is attributable to a Q^4 (3Zn or 4Zn) configuration surrounded only by Zn atoms. However, the presence of the three components for peak **A** suggests Al−O−Al connectivity between adjacent AlO_4 tetrahedra,[21] the configuration of which is represented as $Q^3(m\text{Al}, (3-m)\text{Zn})$ (m = 1, 2, 3) and $Q^4(m\text{Al}, (4-m)\text{Zn})$ (m = 1, 2, 3, 4). The true m value is unclear at present; however, the results suggest that Al atoms may be present simultaneously at adjacent Zn/Al sites to the extent that the occupancy allows.

By contrast, the resonance peak **B** was fitted by a single peak at δ_{iso} = 88.3 ppm, which is not a usual δ value for AlO_4 and is shifted considerably to the downfield side as shown in Figure 5b. The same tendency that the chemical shift, δ, increases with increasing Al−O−Ba connectivity for AlO_4 tetrahedra, which has been reported in the spectra of Al_2O_3−BaO glasses.[22] The four crystallographic Zn/Al sites determined by the structural analysis must be assigned to the two peaks **A** and **B**; however, at present, we could not unambiguously

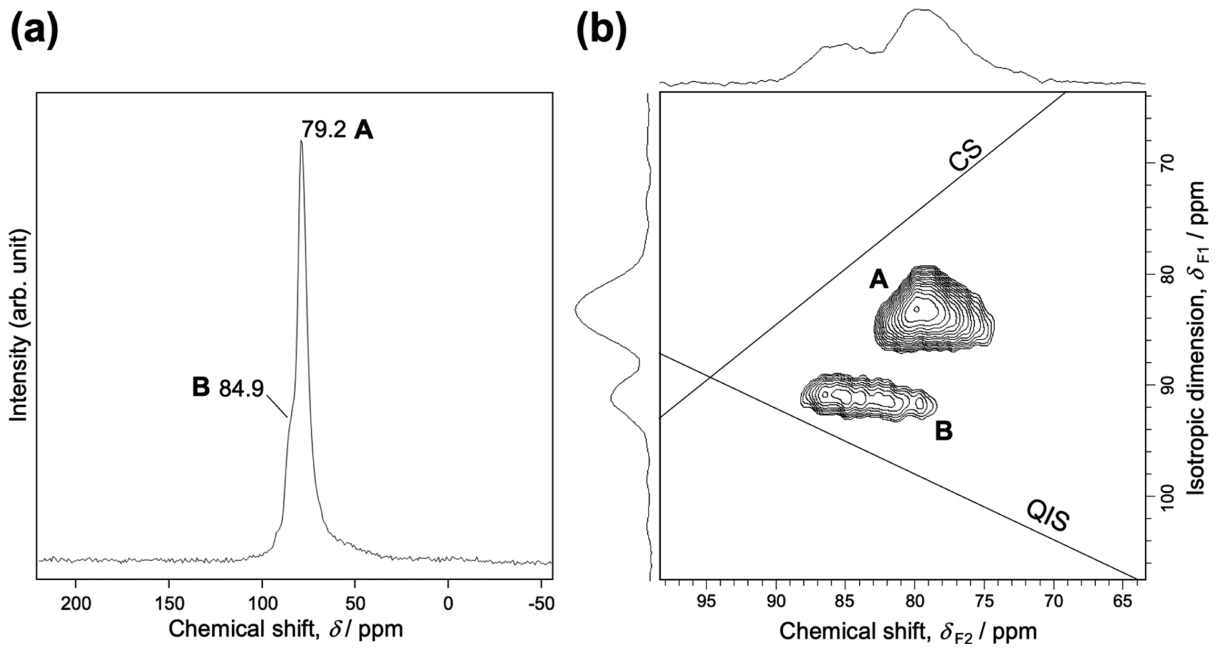

Figure 5. (a) ^{27}Al DE-MAS NMR spectrum and (b) sheared z-filtered ^{27}Al 3QMAS NMR spectrum for $Ba_{33}Zn_{22}Al_8O_{67}$. CS and QIS axes indicate the chemical shift and quadrupolar-induced shift axes, respectively.

https://doi.org/10.1021/acsomega.1c05190
ACS Omega 2021, 6, 30140−30147

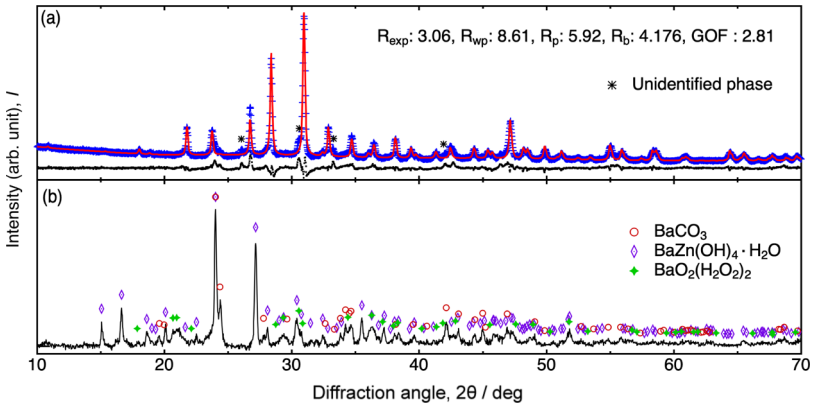

Figure 6. Powder XRD patterns for the sample synthesized by heating at 1323 K for 2 h in a dry airflow: (a) as-prepared sample and (b) sample left in air with 60% relative humidity for 1 day. Detailed Rietveld result is shown in Figure S1.

determine the distribution of Al atoms because all of the Al atoms partially occupy the Zn sites. However, peak **B** might be assignable to Q^1(0Al, 1Zn) or Q^1(1Al, 0Zn) of Zn/Al4 in the $\{Ba4[Zn/Al4O_4]_4\}$ motif with a probability of 0.5, three of whose bridging O atoms connect to Ba at Ba4. The **A** peaks, as previously mentioned, might be assignable to Q^3(mAl, (3-m) Zn) (m = 1, 2, 3) and Q^4(mAl, (4 − m)Zn) (m = 1, 2, 3, 4) for the other Zn/Al sites: Zn/Al2, Zn/Al3, and Zn/Al5 in the $\{[O6(Zn/Al2)_4][Zn/Al3O_4]_4\}$ motif and Zn/Al4 in the $\{[O1(Zn1)_4][Zn/Al4O_4]_4\}$ motif with a probability of 0.5. Ultra-high-magnetic-field solid-state ^{27}Al and ^{67}Zn NMR measurements would be helpful for further elucidating the distributions of Al and Zn atoms; however, such measurements are left for future work.

2.3. Polycrystalline Sample Preparation. Figure 6a shows a powder XRD pattern for a disk sample prepared by heating the compact of the starting mixture with a Ba/Zn/Al molar ratio of 33:22:8 at 1323 K for 2 h under dry flowing air. The diffraction angles and relative intensities of the XRD peaks in the pattern are explained by the crystal structure of $Ba_{33}Zn_{22}Al_8O_{67}$, except for a few unidentified small peaks indicated with asterisks (*) in the figure. When the sample was left in air with a humidity of 60% for 1 day, it reacted with H_2O and CO_2 in air and decomposed into $BaCO_3$, $BaZn(OH)_4 \cdot H_2O$, and $BaO_2(H_2O_2)_2$ (Figure 6b). The handling and storage of $Ba_{33}Zn_{22}Al_8O_{67}$ must be carried out in a dry atmosphere.

2.4. Melting Point and Thermal Expansion. The melting temperature of $Ba_{33}Zn_{22}Al_8O_{67}$, as measured by differential thermal analysis (DTA) of the fragments of the disk sample, was 1452 K. A linear thermal expansion coefficient of 10.4 × 10^{-6} K^{-1} from 301 to 873 K was obtained for a polycrystalline square-rod sample (13.80 mm × 3 mm × 3 mm, ∼73% relative density). This coefficient is similar to those reported for alumina [(7−9) × 10^{-6} K^{-1}] and cubic zirconia [(8−10) × 10^{-6} K^{-1}].[23,24]

2.5. Electronic Properties. The temperature dependence of the electrical resistivity was measured for the disk sample of $Ba_{33}Zn_{22}Al_8O_{67}$ (5 mm in diameter, 2.2 mm in thickness, and ∼70% relative density); the results are shown in Figure 7. The electrical conductivities obtained by the impedance method at 1073 K under dry and wet airflows were 6.2 × 10^{-7} and 2.9 × 10^{-6} S cm^{-1}, respectively. These values agree with the conductivities measured by the direct current two-terminal method at the same temperature. The activation energies for the conductivity in the temperature range from 923 to 1073 K under dry and wet airflows were estimated to be 0.65 and 0.59

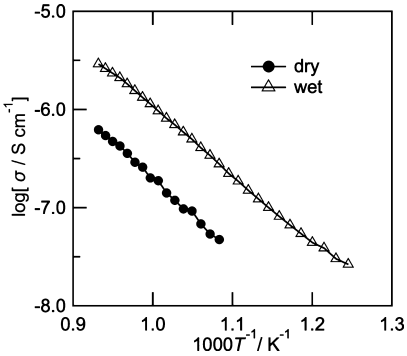

Figure 7. Temperature dependence of electrical conductivity, σ, for $Ba_{33}Zn_{22}Al_8O_{67}$. Open triangles and solid circles indicate the results obtained under wet and dry airflows, respectively.

eV, respectively. After the conductivity measurement in the wet airflow in the temperature range 923−1073 K, the samples were subjected to the dry airflow and their conductivities decreased to the same values previously measured in the dry airflow. The increase in the conductivity of the sample in the wet airflow might be attributable to the contribution of proton conduction.

The relative permittivities of the disk sample measured at 1 MHz in the temperature range 298−400 K and with the sample in the dry airflow are shown in Figure 8. The relative

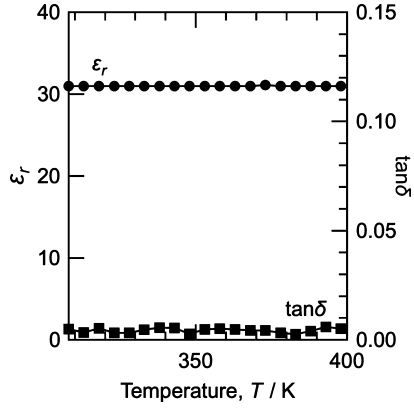

Figure 8. Temperature dependence of relative permittivity, ε_r, and dielectric loss, tanδ, measured for $Ba_{33}Zn_{22}Al_8O_{67}$ at 1 MHz in a dry airflow.

https://doi.org/10.1021/acsomega.1c05190
ACS Omega 2021, 6, 30140−30147

permittivity at 301 K was 31. The dielectric loss, tan δ, was approximately constant and less than 0.01 (Figure 8). The temperature coefficient of the relative permittivity change at 1 MHz in the dry airflow was approximately 15 ppm K^{-1} at 301 K.

3. SUMMARY

A novel quaternary compound, $Ba_{33}Zn_{22}Al_8O_{67}$, having a three-dimensional network structure formed by sharing the vertex O atoms of Zn/AlO_4 tetrahedra, was synthesized in the Ba−Al−Zn−O system. The melting temperature of the compound, as measured by DTA, was 1452 K. A single crystal obtained from a melted and solidified sample was used for XRD measurements. The crystal structure of $Ba_{33}Zn_{22}Al_8O_{67}$ (cubic, a = 16.3372(4) Å, space group $F23$), was explained on the basis of motifs of $\{[OZn_4][Zn/AlO_4]_4\}$ and $\{[O(Zn/Al)_4][Zn/AlO_4]_4\}$. An O-centered Zn tetrahedron $[OZn_4]$ or Zn/Al tetrahedron $[O(Zn/Al)_4]$ is present at the center of the motifs. The $[OZn_4]$ tetrahedron is statistically replaced by a Ba atom with a probability of 0.5 and another motif of $\{[Ba][Zn/AlO_4]_4\}$ is formed. The $\{[O(Zn/Al)_4][Zn/AlO_4]_4\}$ and/or $\{[Ba][Zn/AlO_4]_4\}$ motifs are connected to each other by sharing the apical O atoms of Zn/AlO_4 tetrahedra. The $\{[OZn_4][Zn/AlO_4]_4\}$ or $\{[Ba][Zn/AlO_4]_4\}$ motifs and the $\{[O(Zn/Al)_4][Zn/AlO_4]_4\}$ motifs alternatingly align along the a-axis direction, and Ba atoms are situated between the motifs. The ^{27}Al MAS NMR spectra show two types of resonance peaks with a δ_{iso} of ∼82 ppm (peak **A**) and δ_{iso} = 88.3 ppm (peak **B**). In addition, ^{27}Al 3QMAS NMR spectra show that peak **B** corresponds to a single Al site, whereas the broad peak **A** represents multiple Al sites. The two peaks could be assigned to the $Al(OZn)_4$ or $Q^n(mAl)$ configuration with Al−O−Al connectivity (peak **A**) and the Q^1(0Al 1Zn) or Q^1(1Al 0Zn) configuration connecting to the Ba site (peak **B**).

To the best of our knowledge, the statistical substitution of a Ba atom for an O-centered Zn tetrahedron $[OZn_4]$ has not been reported in any other oxides. Polycrystalline samples of $Ba_{33}Zn_{22}Al_8O_{67}$ were prepared by solid-state reaction in a dry airflow. A linear thermal expansion coefficient of 10.4×10^{-6} K^{-1} was measured for a polycrystalline sample in the temperature range 301−873 K. $Ba_{33}Zn_{22}Al_8O_{67}$ could be handled below 30% relative humidity at room temperature; however, it changed to hydroxides, hydrates, and barium carbonate in wet air when the relative humidity was greater than 30%. The electrical conductivities in dry and wet airflows at 1073 K were 6.2×10^{-7} and 2.9×10^{-6} S cm^{-1}, respectively. A relative permittivity of 31 and a temperature coefficient of 15 ppm K^{-1} were measured at 1 MHz and 301 K in a dry airflow.

4. EXPERIMENTAL SECTION

$BaCO_3$ (Hakushin Chemical Laboratory, 98%), ZnO (Mitsui Kinzoku, 99.9%), and Al_2O_3 (Sumitomo Chemical, 99.99%) powders were weighed out in a Ba:Zn:Al molar ratio of 1:7:2 and mixed using an agate mortar and pestle. The mixed powder was pressed to form a rod with a diameter and length of 8 and 50 mm, respectively, using a cold isostatic pressing machine (Rikenkiki S1-150). A part of the pressed rod was melted and solidified in an atmospheric gas flow [Taiyo Nippon Sanso, high purity (Grade 1)] at 500 mL min^{-1} using a floating zone furnace (ASGAL, FZ-SS35WV). Single-crystal fragments were cut from a transparent part of the solidified rod in a glovebox (MBRAUN Labmaster130) filled with Ar gas (Taiyo Nippon Sanso, 99.9999%). Some of the single-crystal fragments were embedded in resin and polished. After the polished surface was coated with carbon, the chemical composition of the single crystals was analyzed by EPMA (JEOL JXA-8200). A single-crystal fragment was sealed in a glass capillary with a 0.5 mm inner diameter in the glovebox, and single-crystal XRD measurements were performed (Bruker D8 QUEST; Mo Kα). The crystal structure was analyzed using the APEX III[25] and SHELXL-2014 programs[26] and was visualized using the VESTA program.[27]

After $BaCO_3$, ZnO, and Al_2O_3 powders were weighed out in a Ba:Zn:Al cation molar ratio of 33:22:8, which was determined by single-crystal X-ray structure analyses and EPMA using the single crystal sample of the new oxide, the powders were mixed and pressed into disk-shaped compacts with a diameter of 6 mm and into cuboids with dimensions of 3 mm × 3 mm × 14 mm using molds and a uniaxial pressurizer (∼5 MPa). The compacts were placed in an alumina crucible with a lid (Nikkato, SSA-S, 99.6%, 46 mm outer diameter, and 36 mm height) and heated to 1323 K for 3 h in a dry airflow at a rate of 50 mL min^{-1}. The dry airflow was prepared by passing air through a silica-gel-filled container (approximately 30% relative humidity) using an aeration pump (Asone, SA-2000S). The temperature was maintained at 1323 K for 2 h and then the power to the furnace was shut off. After cooling to room temperature, a part of the sample was crushed into powder for XRD analysis (Bruker D2 Phaser, Cu Kα). The crystalline phases that generated peaks in the XRD patterns were identified using TOPAS software.[28]

The local structure around Al atoms was investigated using solid-state magic angle spinning (MAS) NMR measurements. An ^{27}Al directly excited (DE) MAS NMR spectrum was recorded under a 9.4 T magnetic field (Bruker Biospin K.K., Japan, AVANCEIII 400WB) at a resonance frequency of 104.267 MHz using a 3.2 mm VT-MAS probe with a zirconia rotor. An ^{27}Al 3QMAS two-dimensional (2D) NMR spectrum was also recorded using a z-filter and a $\{^1H\}$ decoupling sequence. The rotor spinning rate was set at 24 kHz for the acquisition of both spectra. A 1.0 M $AlCl_3$ solution was used as a secondary reference material for the chemical shift of ^{27}Al nuclei.

DTA (NETZSCH, STA2500) was carried out for small fragments of a crushed disk-shaped sample. The fragments were placed in an alumina cell with a diameter of 5 mm and a height of 5 mm. A dilatometer (DIL; Bruker, TD5000SA) was used to measure the linear thermal expansion of the square-rod-shaped sample in the temperature range from 301 to 873 K (ramp rate of 20 K min^{-1}) under an Ar flow at 50 mL min^{-1} (Taiyo Nippon Sanso, 99.9999%).

The impedance of the disk sample was measured in the temperature range from 873 to 1073 K in dry and wet airflows with a flow rate of 200 mL min^{-1} using an LCR meter (Hioki, 3536) and Au electrodes were prepared by heating Au paste (Furuya Metal) at 1073 K for 30 min. The wet airflow was prepared by bubbling air through water at 298 K (∼3.2 kPa saturated water vapor pressure) using the aeration pump. The electrical conductivity was determined from Cole−Cole plots of the recorded impedance data. The resistivity was confirmed via the direct current two-terminal method using a digital multimeter (Keithley, 2000). The capacitance and dielectric loss for the disk sample were measured at 1 MHz from 298 to 400 K using the LCR meter.

https://doi.org/10.1021/acsomega.1c05190
ACS Omega 2021, 6, 30140−30147

■ ASSOCIATED CONTENT

Supporting Information

The Supporting Information is available free of charge at https://pubs.acs.org/doi/10.1021/acsomega.1c05190.

Atomic displacement parameters, interatomic distances, isotropic chemical shifts, quadrupolar coupling constants, asymmetry parameters, and result of Rietveld analysis (PDF)

Crystallographic data (CIF)

■ AUTHOR INFORMATION

Corresponding Author

Rayko Simura − *Institute of Multidisciplinary Research for Advanced Materials, Tohoku University, Aobaku Sendai, Miyagi 980-8577, Japan;* orcid.org/0000-0003-1760-4030; Email: ray@tohoku.ac.jp

Authors

Kyosuke Sawamura − *Institute of Multidisciplinary Research for Advanced Materials, Tohoku University, Aobaku Sendai, Miyagi 980-8577, Japan; Department of Metallurgy, Materials Science and Materials Processing, Graduate School of Engineering, Tohoku University, Sendai 980-8579, Japan*

Hisanori Yamane − *Institute of Multidisciplinary Research for Advanced Materials, Tohoku University, Aobaku Sendai, Miyagi 980-8577, Japan*

Takuji Ikeda − *Research Institute for Chemical Process Technology, National Institute of Advanced Industrial and Science and Technology, Sendai 983-8551, Japan;* orcid.org/0000-0001-7992-5636

Complete contact information is available at: https://pubs.acs.org/10.1021/acsomega.1c05190

Notes

The authors declare no competing financial interest.

■ ACKNOWLEDGMENTS

We thank M. Takaishi for assistance with a part of the synthesis and preparation of samples, T. Sugawara [Institute for Materials Research (IMR), Tohoku University] for preparing a melt-solidified sample with a floating zone furnace under the CRDAM-IMR, Tohoku University (Proposal no. 202012-CRKEQ-0208), and T. Kamaya [Institute of Multidisciplinary Research for Advanced Materials (IMRAM), Tohoku University] for EPMA measurements. This work was supported by JSPS KAKENHI Grant Number JP18H05347 and by the Dynamic Alliance for Open Innovation Bridging Human, Environment and Materials in the Network Joint Research Center for Materials and Devices.

■ REFERENCES

(1) West, A. R. Crystal chemistry of some tetrahedral oxides. *Z. Kristallogr.* **1975**, *141*, 422−436.

(2) Wells, A. F. Survey of tetrahedral structures. *Philos. Trans. R. Soc., A* **1986**, *319*, 291−335.

(3) Müller-Buschbaum, H. Zur kristallchemie von alkali-, erdalkali- und seltenerdmetall-oxozinkaten. *Z. Anorg. Allg. Chem.* **2010**, *636*, 275−295.

(4) Krivovichev, S. V.; Mentré, O.; Siidra, O. I.; Colmont, M.; Filatov, S. K. Anion-centered tetrahedra in inorganic compounds. *Chem. Rev. (Washington, DC, U. S.)* **2013**, *113*, 6459−6535.

(5) Bakakin, V. V.; Seryotkin, Y. V. Two groups of compounds with large porous superframeworks based on anion-centered $[OT_4]$ tetrahedra and the features of their extraframework subsystems. *J. Struct. Chem.* **2020**, *61*, 1072−1079.

(6) Harrison, W. T. A.; Broach, R. W.; Bedard, R. A.; Gier, T. E.; Bu, X.; Stucky, G. D. Synthesis and characterization of a new family of thermally stable open-framework zincophosphate/ arsenate phases: $M_3Zn_4O(XO_4)_3{\cdot}nH_2O$ (M = Na, K, Rb, Li, ...; X = P, As; n = ∼3.5—6). Crystal structures of $Rb_3Zn_4O(PO_4)_3{\cdot}3.5H_2O$, $K_3Zn_4O(AsO_4)_3{\cdot}4H_2O$, and $Na_3Zn_4O(PO_4)_3{\cdot}6H_2O$. *Chem. Mater.* **1996**, *8*, 691−700.

(7) Khoury, H. N.; Sokol, E. V.; Kokh, S. N.; Seryotkin, Y. V.; Nigmatulina, E. N.; Goryainov, S. V.; Belogub, E. V.; Clark, I. D. Tululite, $Ca_{14}(Fe^{3+},Al)(Al,Zn,Fe^{3+},Si,P,Mn,Mg)_{15}O_{36}$: a new Ca zincate-aluminate from combustion metamorphic marbles, central Jordan. *Mineral. Petrol.* **2015**, *110*, 125−140.

(8) Barbanyagre, V. D.; Timoshenko, T. I.; Ilyinets, A. M.; Shamshurov, V. M. Calcium aluminozincates of $Ca_xAl_yZn_kO_n$ composition. *Powder Diffr.* **1997**, *12*, 22−26.

(9) Istomin, S. Y.; Chernov, S. V.; Antipov, E. V.; Dobrovolsky, Y. A. Composition-induced phase transition in $Ca_{14}Zn_{6-x}Ga_{10+x}O_{35+x/2}$ (x=0.0 and 0.5). *J. Solid State Chem.* **2007**, *180*, 1882−1888.

(10) BrukerAXS.Inc. *SMART, SAINT and SADABS*: Madison, Wisconsin, USA, 1997.

(11) Parsons, S.; Flack, H. D.; Wagner, T. Use of intensity quotients and differences in absolute structure refinement. *Acta Crystallogr., Sect. B: Struct. Sci., Cryst. Eng. Mater.* **2013**, *69*, 249−259.

(12) Shannon, R. D. Revised effective ionic radii and systematic studies of interatomic distances in halides and chalcogenides. *Acta Crystallogr., Sect. A: Cryst. Phys., Diffr., Theor. Gen. Crystallogr.* **1976**, *32*, 751−767.

(13) Larsson, A.-K.; Withers, R. L.; Perez-Mato, J. M.; Fitz Gerald, J. D.; Saines, P. J.; Kennedy, B. J.; Liu, Y. On the microstructure and symmetry of apparently hexagonal $BaAl_2O_4$. *J. Solid State Chem.* **2008**, *181*, 1816−1823.

(14) von Schnering, H. G.; Hoppe, R.; Zemann, J. Die Kristallstruktur des $BaZnO_2$. *Z. Anorg. Allg. Chem.* **1960**, *305*, 241−254.

(15) Saradhi, M. P.; Raveau, B.; Caignaert, V.; Varadaraju, U. V. Multiband orange−red photoluminescence of Eu^{3+} ions in new "114" $LnBaZn_3GaO_7$ and $LnBaZn_3AlO_7$ oxides. *J. Solid State Chem.* **2010**, *183*, 485−490.

(16) Cuartero, V.; Blasco, J.; Subías, G.; García, J.; Rodríguez-Velamazán, J. A.; Ritter, C. Structural, magnetic, and electronic properties of $CaBaCo_{4-x}M_xO_7$ (M = Fe, Zn). *Inorg. Chem.* **2018**, *57*, 3360−3370.

(17) Valldor, M. Syntheses and structures of compounds with $YBaCo_4O_7$-type structure. *Solid State Sci.* **2004**, *6*, 251−266.

(18) Kemmitt, T.; Ingham, B.; Linklater, R. Optimization of sol−gel-formed ZnO:Al processing parameters by observation of dopant ion location using solid-state ^{27}Al NMR spectrometry. *J. Phys. Chem. C* **2011**, *115*, 15031−15039.

(19) Straube, T.; Linders, J.; Mayer-Gall, T.; Textor, T.; Mayer, C.; Gutmann, J. S. Polyol synthesized aluminum doped zinc oxide nanoparticles - influence of the hydration ratio on crystal growth, dopant incorporation and electrical properties. *Mater. Today: Proc.* **2017**, *4*, S253−S262.

(20) Avadhut, Y. S.; Weber, J.; Hammarberg, E.; Feldmann, C.; Schmedt auf der Günne, J. Structural investigation of aluminium doped ZnO nanoparticles by solid-state NMR spectroscopy. *Phys. Chem. Chem. Phys.* **2012**, *14*, 11610−11625.

(21) Müller, D.; Gessner, W.; Samoson, A.; Lippmaa, E.; Scheler, G. Solid-state aluminium-27 nuclear magnetic resonance chemical shift and quadrupole coupling data for condensed AlO_4 tetrahedra. *J. Chem. Soc., Dalton Trans.* **1986**, 1277−1281.

(22) Licheron, M.; Montouillout, V.; Millot, F.; Neuville, D. R. Raman and ^{27}Al NMR structure investigations of aluminate glasses: $(1-x)Al_2O_3$—x MO, with M=Ca, Sr, Ba and $0.5<x<0.75$). *J. Non-Cryst. Solids* **2011**, *357*, 2796−2801.

(23) Whittemore, O. J.; Ault, N. N. Thermal expansion of various ceramic materials to 1500 °C. *J. Am. Ceram. Soc.* **1956**, *39*, 443−444.

(24) Kirchner, H. P. The thermal expansion of ceramic crystals. *Prog. Solid State Chem.* **1964**, *1*, 1−36.
(25) BrukerAXS.Inc. *Program APEX III, 3*; Bruker AXS Inc., 2012.
(26) Sheldrick, G. M. Crystal structure refinement with SHELXL. *Acta Crystallogr., Sect. C: Struct. Chem.* **2015**, *71*, 3−8.
(27) Momma, K.; Izumi, F. VESTA 3 for three-dimensional visualization of crystal, volumetric and morphology data. *J. Appl. Crystallogr.* **2011**, *44*, 1272−1276.
(28) Coelho, A. A. TOPAS and TOPAS-Academic: an optimization program integrating computer algebra and crystallographic objects written in C++. *J. Appl. Crystallogr.* **2018**, *51*, 210−218.

https://doi.org/10.1021/acsomega.1c05190
ACS Omega 2021, 6, 30140−30147